Journal of Materials Science: Materials in Electronics (2020) 31:14930–14940
https://doi.org/10.1007/s10854-020-04054-7

The potentials of TiO_2 nanocatalyst on HMX thermolysis

Sherif Elbasuney[1,2] · **Gharieb S. El-Sayyad**[2,3]

Received: 17 April 2020 / Accepted: 21 July 2020 / Published online: 30 July 2020

Abstract

Even though HMX is one of the most powerful highly explosive materials; HMX-based propellants demonstrated complexity of burning rate control as well as high pressure exponent (n). In addition, HMX is insensitive to common catalyst. TiO_2 can offer novel catalyzing ability for HMX. Highly-crystalline, mono-dispersed TiO_2 NPs of 5.0 nm particle size with proper surface area (26.87 ± 0. 36 m^2/g) were fabricated using hydrothermal processing. TiO_2 NPs were re-dispersed in organic solvent and effectively-integrated into HMX via co-precipitation technique; the impact of TiO_2 NPs on HMX thermal behavior was investigated using DSC and TGA. TiO_2 NPs exposed superior catalytic performance; the endothermic phase change of HMX at 187 °C was decreased by 43.3%. The main exothermic decomposition peak was decreased by 10 °C with enhanced total heat release by 46.7%. The catalytic performance of TiO_2 NPs could be ascribed to the release of active surface $\dot{\mathbf{O}}\mathbf{H}$ radicals that could induce HMX decomposition via hydrogen abstraction. Furthermore, TiO_2 NPs could adsorb evolved NO_2 on its surface with surge in total heat release in condensed phase.

1 Introduction

HMX is one of the most vigorous explosive materials in terms of heat output and gaseous products [1, 2]. HMX can offer large volume of gaseous products at low molecular weight [3–6]. Therefore, HMX has found wide applications in solid rocket propellant [7–9]. It was reported that HMX is insensitive to traditional catalysts [10]. The main approach that could affect thermolysis of HMX includes hydrogen atom abstraction with heterocyclic ring cleavage [11, 12].

Transition metal oxides were reported to have catalytic influence on HMX thermolysis with decrease in its onset decomposition temperature [7, 13]. Nanopowders, with increased surface areas, are promising materials for catalytic applications of different energetic systems [14]. High catalytic effect on HMX was reported through TiO_2 NPs. HMX catalyzation includes a decrease in onset decomposition temperature, high reaction rate, and decrease in pressure exponent value [15–17]. These effects could be achieved using TiO_2 NPs. Enhanced catalytic performance could be accomplished with particle size decrease [18–20].

Some metal oxide nanocomposites were prepared by different green methods which are used for the catalytic performance and other critical applications. Sol–gel, sol–gel-hydrothermal, and photo-deposition methods were used to synthesize pure TiO_2, PdO/TiO_2, and Pd/TiO_2 nanostructures. Citric acid was used as a stabilizer, reducing, and capping agent, since it is green, available, clean, and nontoxic [21].

A study conducted by Safajou et al. [22] shows that TiO_2 nanowire (NWs) was prepared by an alkaline hydrothermal process and the following formula Graphene/Pd/TiO_2 NPs and Graphene/Pd/TiO_2-NWs were synthesized by a combination of hydrothermal and photo-deposition methods. The synthesized nanocomposites were investigated for their enhanced photocatalytic degradation of dyes.

Also, photo-degradation of methylene blue was investigated by the utilization of the mixed metal oxides such as Fe_2O_3–TiO_2 NPs, TiO_2@SiO_2 core/shell NPs and N-doped graphene quantum dot/TiO_2 nanocomposite [23–25]. Finally, the photocatalytic degradation of azo dyes using TiO_2 NPs

---

✉ Sherif Elbasuney
sherif_basuney2000@yahoo.com; s.elbasuney@mtc.edu.eg

✉ Gharieb S. El-Sayyad
Gharieb.Elsayyad@eaea.org.eg

[1] Head of Nanotechnology Research Center, Military Technical College (MTC), Cairo, Egypt

[2] School of Chemical Engineering, Military Technical College (MTC), Egyptian Armed Forces, Cairo, Egypt

[3] Drug Radiation Research Department, National Center for Radiation Research and Technology (NCRRT), Egyptian Atomic Energy Authority (EAEA), Cairo, Egypt

supported Ag NPs which prepared by a green method was investigated by Rostami-Vartooni et al. [26].

Different chemical methods such as successive ion layer adsorption and reaction, chemical bath deposition, microwave, and hydrothermal served to deposition of CdS on the prepared TiO_2 surface for use in different optoelectronic fields. TiO_2/CdS nanocomposite was synthesized by hydrothermal method and was then deposited on the FTO surface to investigate their influences on the dye-sensitized solar cell performance [27]. Also, TiO_2 NPs were prepared using tripodal tetra-amine ligands (complexing agent) by two-step sol–gel method for the application in dye-sensitized solar cells [28]. The effect of the ligand on the synthesis of different metal oxide NPs must be taken into consideration, and the size and optical properties of TiO_2 NPs in a two-step sol–gel method was altered after the use of Schiff base ligands [29]. Also, the effect of tertiary amines on the synthesis and photovoltaic properties of TiO_2 NPs in dye-sensitized solar cells was investigated [30]. Finally, a stable plasmonic-improved dye-sensitized solar cells was achieved by Ag NPs between TiO_2 Layers [31].

It must be noted that, the as-fabricated mesoporous TiO_2 fibers exhibit much higher photocatalytic activity and stability than both the conventional solid counterparts and the commercially-available P25. The abundant vapors released from the introduced foaming agents are responsible for the creation of pores with uniform spatial distribution in the spun precursor fibers [32]. In another study regarding nanomaterials-based TiO_2 NPs, a novel and highly efficient visible-light-driven photocatalyst with robust stability made up of thoroughly mesoporous $TiO_2/WO_3/g\text{-}C_3N_4$ ternary hybrid nanofibers and TiO_2/CuO/Cu had been fabricated through a foaming-assisted electro-spinning process followed by a solution-dipping process [33, 34]. Finally, a brilliant $BiVO_4@TiO_2$ core–shell hybrid mesoporous nanofiber was used for efficient visible-light-driven photocatalytic hydrogen production [35].

1.1 TiO_2 catalyzation mechanism

It is widely established that nitramine decomposition can be catalyzed with $\dot{\mathbf{O}}\mathbf{H}$ radicals. TiO_2 NPs are characterized with hydrous surface (surface-bound hydroxyl groups). The release of surface $\dot{\mathbf{O}}\mathbf{H}$ radicals can speed up HMX decomposition [36]. The required activation energy to liberate $\dot{\mathbf{O}}\mathbf{H}$ radicals from TiO_2 surface is 65 kJ/mol; this value could decrease with the increase in the particle surface area [16]. Furthermore, NPs surface could absorb gaseous products offering high heat output [20]. TiO_2 NPs could lower the required activation energy for HMX decomposition. Whereas HMX normal decomposition process include C-N bond breakage of heterocyclic ring, decomposition of catalyzed HMX with nanocatalyst includes dehydration of catalyst surface with the release of active $\dot{\mathbf{O}}\mathbf{H}$ radicals; these radicals would abstract H-atom from the heterocyclic ring [37].

Therefore, the catalytic decomposition process could take place at lower temperature and with lower activation energy [38]. The strength of surface-bounded –OH groups is a key parameter for the catalytic activity of oxides. Electronegativity of metal cation x_i expresses the capability to withdraw electron pair (Eq. 1).

$$X_i = X_o \cdot (1 - 2n) \tag{1}$$

where x_o and n are electronegativity of metal atom and the metal charge in the oxide state, respectively.

Metal oxide with high X_i have acid properties, whereas oxides with low X_i have base properties. Oxide point of zero charge (isoelectric point) describes the surface acidity; it is equal to the medium acidity in which oxide surface has no electric charge.

TiO_2 NPs were verified to have superior efficiency compared with other oxides as well as microsize TiO_2 [39, 40]. Reliable fabrication of nanoscopic TiO_2 is an urgent demand. There is a vast benefit for synthesis technology that could offer fabrication of TiO_2 NPs with constant product quality. Hydrothermal processing offered consistent fabrication of different oxide particles in dispersion [41].

1.2 Hydrothermal processing

Hydrothermal processing was reported to be a beneficial technology that could offer fabrication of highly crystalline oxides in dispersion [42, 43]. This technology includes direct mixing of metal salt feed with supercritical fluid (ScF),ScF can expose distinctive characteristics in terms of enhanced levels of OH^- [18, 44–48]. Above critical conditions, phase boundary vanishes and a homogenous supercritical phase exists as displayed in Fig. 1 [49, 50].

Oxide fabrication can be achieved via hydrolysis of metal salt with subsequent dehydration step (Eqs. 2 and 3) [52–54].

$$\text{Hydrolysis} : \mathrm{ML}_x + x\mathrm{OH}^- \rightarrow \mathrm{M(OH)}_x + x\,L^- \tag{2}$$

$$\text{Dehydration} : \mathrm{M(OH)}_x \rightarrow \mathrm{MO}_{x/2} + \frac{x}{2}\mathrm{H_2O} \tag{3}$$

Accordingly, this study reports on the consistent fabrication of TiO_2 NPs of 5 nm particle size using hydrothermal synthesis. TiO_2 NPs were developed in dispersion; consequently, colloidal TiO_2 NPs were integrated into HMX particles. Uniform dispersion of TiO_2 NPs into HMX was verified using SEM/mapping technique. The effectiveness of TiO_2 NPs on HMX thermal decomposition was investigated using DSC and TGA. TiO_2 NPs demonstrated superior catalytic efficiency. The endothermic phase change at 187 °C

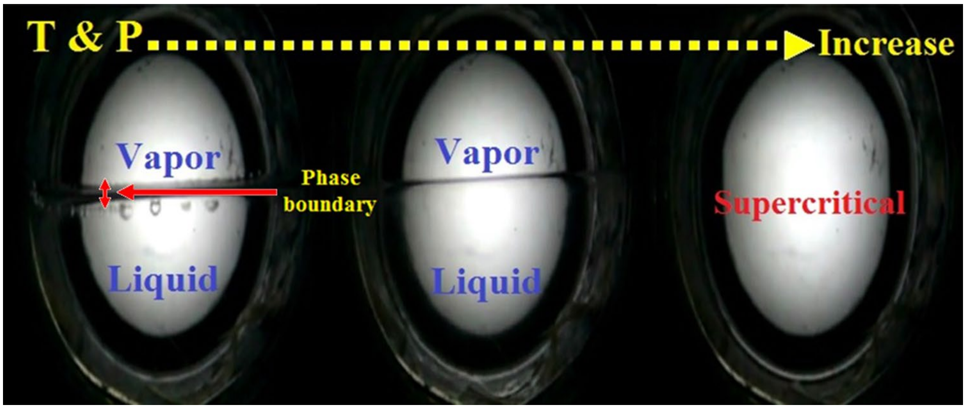

Fig. 1 Phase boundary of ScF with temperature and pressure [51]

was decreased by 43.3%. The exothermic decomposition temperature was decreased by 10 °C with an increase in total heat release by 46.7%. This superior catalytic performance was accomplished at 1 wt % catalyst. TiO_2 NPs catalyzing mechanism was correlated to the release of active surface **$\dot{O}H$** radicals that could attack the heterocyclic ring with hydrogen atom abstraction with heterocyclic ring cleavage.

2 Experimental work

2.1 Hydrothermal synthesis of TiO_2 NPs

The employed metal salt for TiO_2 NP synthesis was titanium (IV) bis (ammonium lactato) dihydroxide ($[CH_3CH(O–)CO_2NH_4]_2Ti(OH)_2$) (TIBALD) 50 wt% in H_2O solution (CAS number 65104-06-5, Aldrich, Germany). ScW was employed at 400 °C, 240 bars (20 ml/min) (Flow A). 0.05 M solution of TIBALD in deionized water was employed at 25 °C, 240 bars (10 ml/min) (Flow B). TiO_2 NPs were developed at the boundary of the flow (Fig. 2). Further details regarding the hydrothermal synthesis of TiO_2 NPs can be observed in the following references [55–58].

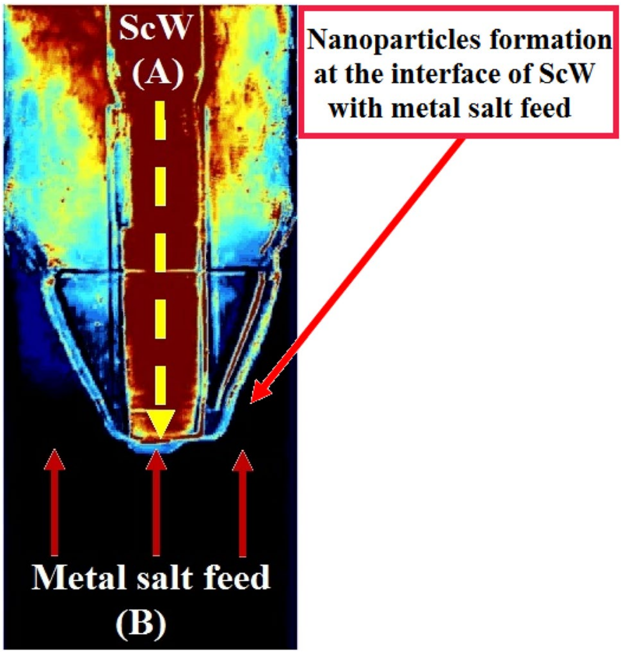

Fig. 2 Schematic for TiO_2 NPs synthesis inside counter-current reactor

2.2 Characterization of TiO_2 NPs

Crystallinity and phase were investigated using X-ray diffraction (XRD) spectroscopy on a Brucker axis D8 diffractometer applying radiation of Cu Kα with ($\lambda = 1.540598$ Å), voltage of 40 kV, and current of 40 mA. The average nanostructure and the particle size determination of the synthesized TiO_2 NPs were determined by applying a High-Resolution Transmission Electron Microscope (HRTEM, JEM2100, Jeol, Japan). The surface morphology and a specific appearance of the dry particles (pure TiO_2 NPs) were examined with Scanning Electron Microscope (SEM, ZEISS, EVO-MA10, Germany). On the other hand, EDX technique (BRUKER, Nano GmbH, D-12489, 410-M, Germany) was applied to investigate the elemental configuration and the atomic percentage of the metals detected in the prepared samples. FTIR spectrometer Nicolet 380 by Thermo-electron Corporation was employed to investigate the nanoparticle chemical structure and their functional groups. Brunauer–Emmett–Teller (BET) method was used to describe the surface area and the measurements were carried out via the surface area analyzer (Nova 3200 Nitrogen Physisorption Apparatus USA) with liquid N_2 as an adsorbate at − 196 °C. Finally, the mapping analysis after applied SEM/EDX technique was used to attain whole information about the clarity, distribution, and the position of the metals (pure TiO_2 NPs) on the surface of HMX.

2.3 Integration of TiO_2 NPs into HMX

All classical NP synthesis techniques include sintering and drying process which result in a dramatic decrease in NP surface area and reactivity. This is the first time ever to report on fabrication of colloidal TiO_2 NPs and their integration into HMX crystalline structure. This approach could offer extensive surface area and reactivity; it could eliminate NP drying and the re-dispersion of dry aggregates.

TiO_2 NPs were decanted from their synthesis medium and re-dispersed in acetone using ultrasonic probe homogenizer. HMX was dissolved in acetone colloid. The ratio of TiO_2 NPs: HMX was 1: 99. TiO_2 NPs were integrated into HMX using co-precipitation technique. The size and shape of TiO_2/HMX hybrid was investigated using SEM/EDX mapping technique for giving further information regarding the simplicity, relationships, and the position of the TiO_2 NPs incorporated with HMX.

2.4 Thermal behavior of catalyzed HMX

Thermal behavior of HMX catalyzed with TiO_2 NPs was investigated using DSC Q20 by TA. Tested sample was heated from 50 to 500 °C. The heating rate was 5 °C/min, under N_2 flow of 50 ml/min. The impact of TiO_2 NPs on HMX weight loss was evaluated using TGA 55 by TA. The tested sample was heated from 50 to 500 °C. The heating rate was 5 °C/min under N_2 flow at 25 ml/min.

3 Result and discussions

3.1 Characterization of the synthesized TiO_2 NPs

TEM micrographs of the synthesized TiO_2 NPs demonstrated mono-dispersed particles with uniform particle size and the particle size was found to be ranging from 3.0 to 10.0 nm with an average particle size recorded at 5.0 nm (Fig. 3a). HRTEM images provided a detailed investigation of structure, shape, and size of TiO_2 NPs which demonstrated a high crystalline structure with spherical and cubic structures (Fig. 3b, c). This result was matched with the results described in previous publications [59–61].

Figure 4 confirmed high-quality mono-dispersed particles and high crystalline structure. The crystalline structure was investigated with X-ray diffraction (XRD). XRD pattern confirmed high-quality anatase crystalline structure (Fig. 4); this is the most common crystalline structure in catalyst applications. For data analysis in Fig. 4, sharp, strong, and intense peaks are observed in $2\Theta = 25.1°$ (101), 28.1° (110), 37.5° (004), 48.9° (200), 54.4° (105), 55.6° (211), and 62.8° (204), while the main peak is located at $2\Theta = 25.4°$, these peaks are in a good matching with those of reference anatase TiO_2 NPs (JCPDS 04-0477) [62]. This result was matched with the results described in previous publications [63–66]. The average crystallite size was calculated using the Debye–Scherrer Eq. (4) [67] and was found to be 10.12 nm:

$$D = \frac{K\lambda}{\beta \cos\theta} \tag{4}$$

where $K = 0.9$ and known as shape factor, λ is x-rays' wavelength (1.54060 Å for Cu-K_α), β is full width at half maximum (FWHM), and θ is the diffraction angle.

SEM image of the fabricated TiO_2 NPs is presented in Fig. 5 a; the synthesized TiO_2 layer appears as a uniform and bright layer, also, the corresponding EDX analysis (Fig. 5b) was similar in words of diffusion (Ti, O, and C atoms) over the grain lines. Also, the carbon atoms were due to the holder which is used in the imaging process [68]. This result was matched with the results described in previous publications [69–72].

FTIR spectrum was a significant study that provides important data about the chemical functional groups

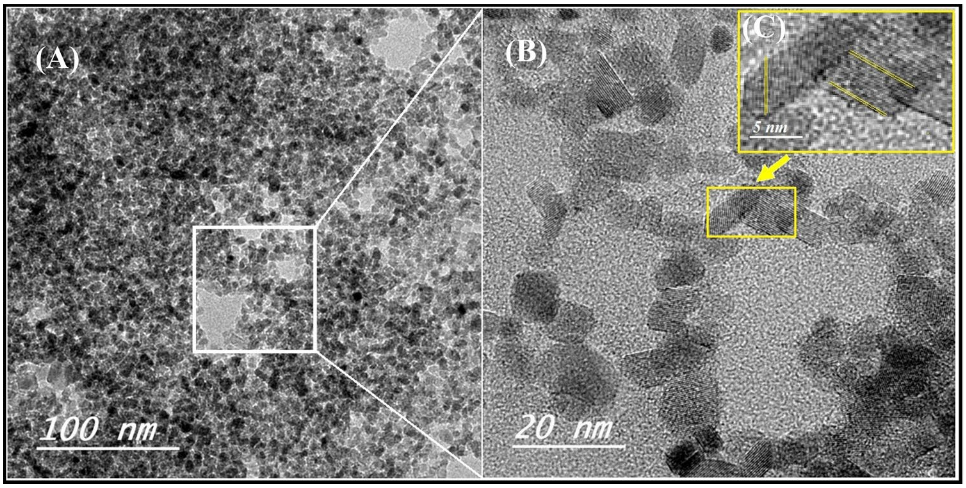

Fig. 3 TEM micrographs of TiO_2 NPs **a** at 100 nm resolution, **b** at 20 nm, and **c** HRTEM at 5 nm

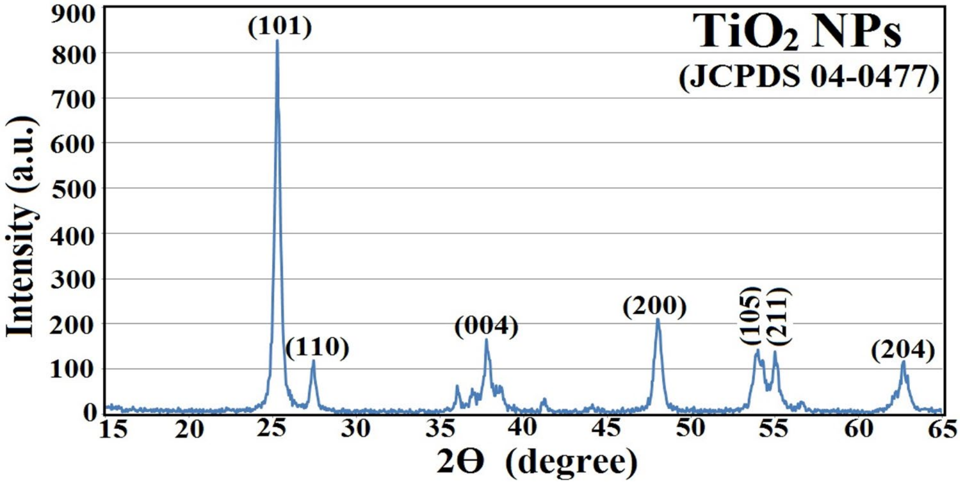

Fig. 4 XRD diffractogram of the synthesized TiO_2 NPs

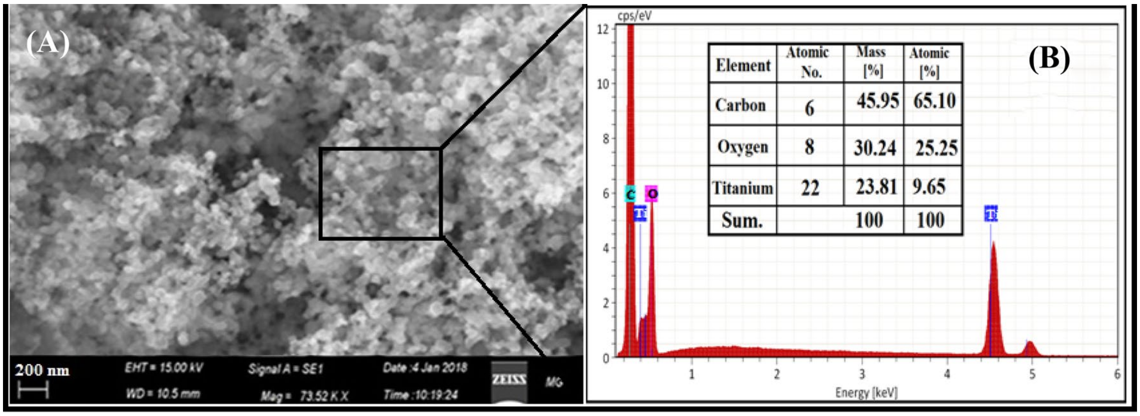

Element	Atomic No.	Mass [%]	Atomic [%]
Carbon	6	45.95	65.10
Oxygen	8	30.24	25.25
Titanium	22	23.81	9.65
Sum.		100	100

Fig. 5 SEM images of the synthesized TiO_2 NPs (**a**) and the corresponding EDX elemental analysis (**b**)

represented in TiO_2 NPs [73]. FTIR spectrum of developed TiO_2 NPs confirmed the hydrous surface. The enhanced levels of IR absorption at 3500 cm^{-1} can be correlated to the O–H surface group stretch as shown in Fig. 6. The antatase Titania appears at the region from 800 to 400 cm^{-1} [74]. This result was matched with the results described in previous publications [75–77].

The electrical and chemical properties are dependent on the specific surface area and grain size, as the chemical and physical phenomena controlled by surface porosity and electrons conduction occur at TiO_2 NP's surface [78]. N_2 adsorption–desorption isotherm of the prepared TiO_2 NPs is shown in Fig. 7.

According to the IUPAC classification, the obtained isotherm was of type (IV), indicating the presence of mesopores. The uptake of adsorbate was increased when pores became filled, and an inflection point occurred near the completion of the first monolayer [62, 77]. From Fig. 7, the calculated surface area of the prepared TiO_2 NPs was $26.87 \pm 0.\ 36$ m^2/g, a similar behavior was detected in the literature and matched our BET result [77, 79–81].

Morphology of TiO_2-HMX nanocomposite was investigated with SEM, to verify the uniform integration of TiO_2 NPs into HMX crystalline structure [82], while EDX examination was performed for its elemental analysis and purity estimation [83–85].

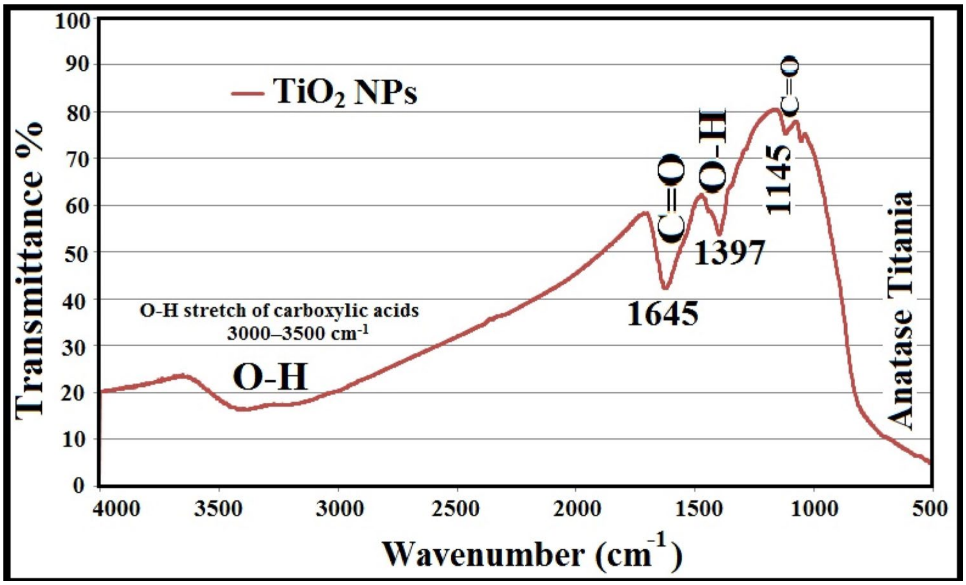

Fig. 6 FTIR spectrum of the synthesized TiO_2 NPs

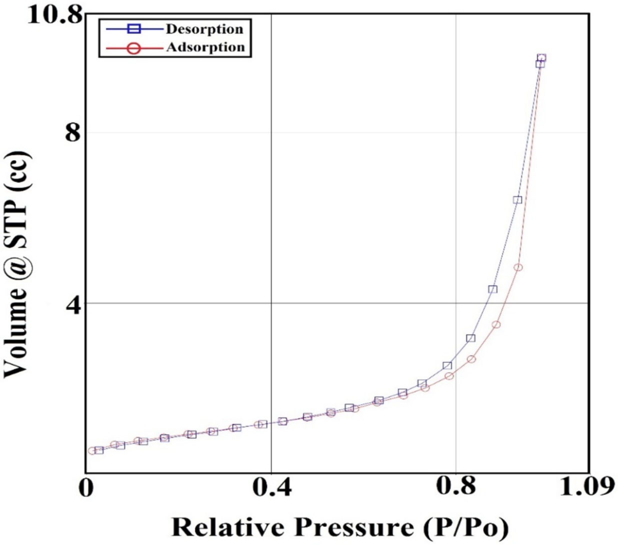

Fig. 7 N_2 Adsorption–desorption isotherm of the prepared TiO_2 NPs

Dry agglomerates include drastic decrease in surface area and reactivity; therefore, the particles would act as micron rather than NPs [44, 54]. Consequently, integration of colloidal particles into HMX could maintain high surface area and reactivity.

Elemental mapping using SEM revealed uniform dispersion of TiO_2 NPs into HMX as shown in Fig. 8. Co-precipitation technique offered uniform dispersion of TiO_2 NPs into HMX. This approach could offer superior interfacial surface area (the calculated surface area of the prepared TiO_2 NPs was 26.87 ± 0. 36 m^2/g; Fig. 7) and catalytic performance. This result was matched with the results described in previous publications [66, 86–89].

3.2 Catalytic activity of TiO_2 NPs

TiO_2 NPs demonstrated dramatic change in HMX thermal behavior. The endothermic phase change of HMX at 187 °C was decreased by 43.3%. The main outcome of this study is that temperature at maximum heat release rate was decreased by 10 °C with an increase in total heat release rate by 46.7% as exhibited in Fig. 9.

The catalytic activity of TiO_2 NPs was further evaluated with TGA. TGA thermogram confirmed DSC outcomes; temperature at total weight loss was decreased by 10 °C as displayed in Fig. 10a and b.

At temperature higher than 150 °C, $\dot{\mathbf{O}}\mathbf{H}$ radicals would be evolved from TiO_2 NPs surface. These active radicals will have high ability to abstract hydrogen from HMX structure [90]. After hydrogen abstraction, energy of N-NO_2 bond would decrease significantly; this could lead to release of nitro group (NO_2) [91]. The evolved NO_2 group could abstract another H-atom from another HMX molecule. Adsorption of NO_2 on the surface of TiO_2 could increase the heat release in condensed phase as shown in Fig. 11 [7].

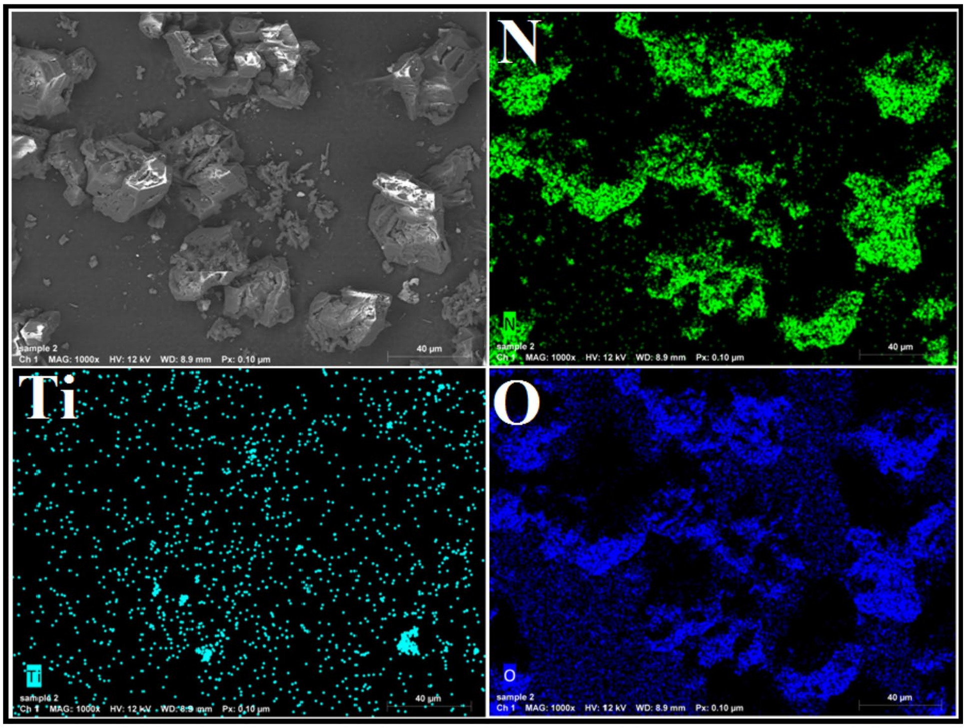

Fig. 8 Elemental mapping of TiO_2 NPs integrated into HMX

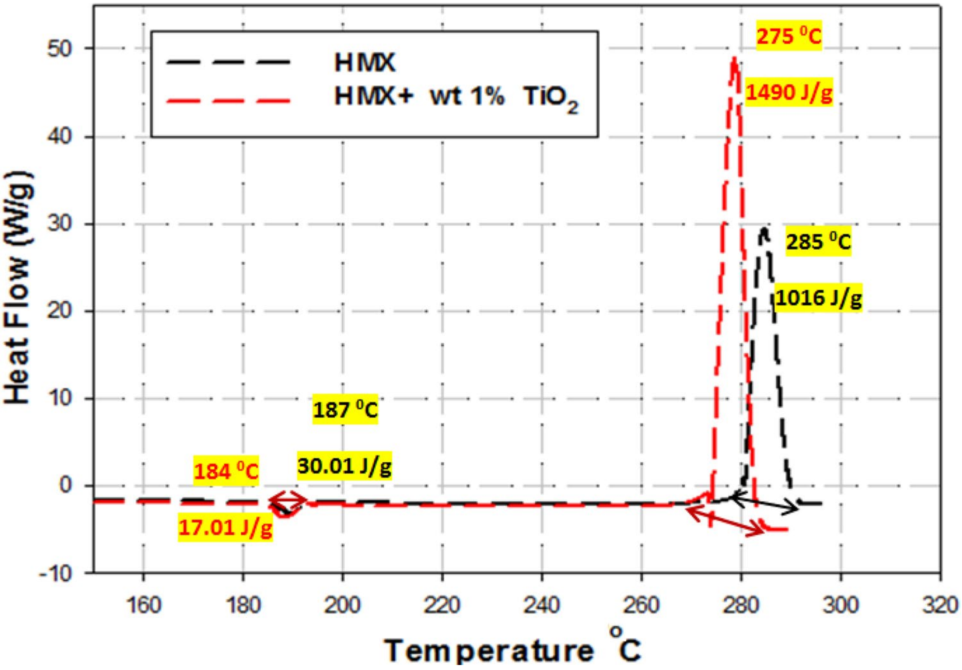

Fig. 9 DSC thermogram of HMX catalyzed with TiO_2 NPs to pure HMX

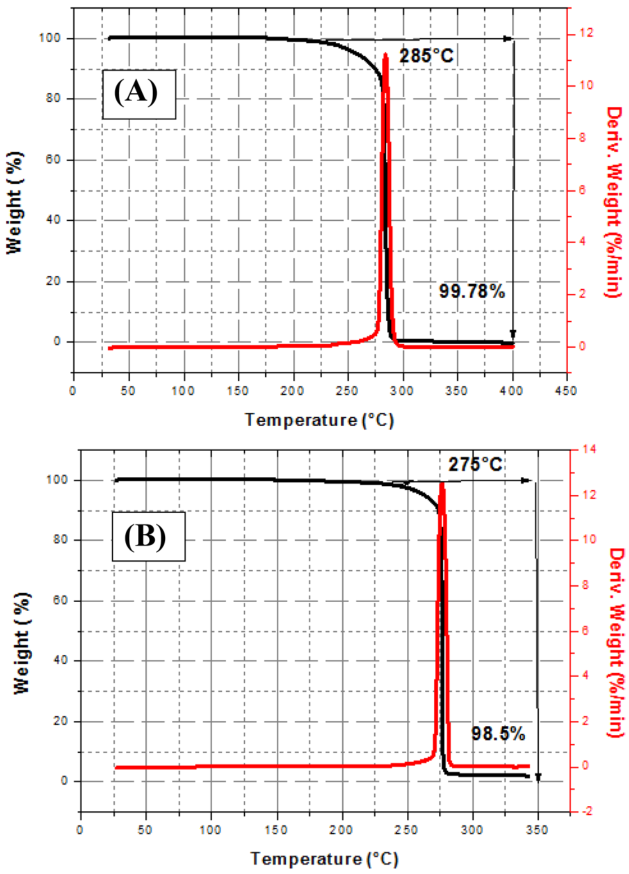

Fig. 10 TGA thermogram of HMX (**a**) and HMX catalyzed with TiO_2 NPs (**b**)

Whereas CH_2O and N_2O fragment will be evolved at low heating rate; HCN and NO_2 will be evolved at high heating rate. Moreover, CH_2O could be due to $\dot{\mathbf{O}}\mathbf{H}$ interaction with double bond. The main TiO_2 NPs catalytic steps include dehydroxylation of the metal oxide surface with the release of active $\dot{\mathbf{O}}\mathbf{H}$ radicals, nitramine decomposition through hydrogen abstraction with $\dot{\mathbf{O}}\mathbf{H}$ radicals, and adsorption of liberated NO_2 on the surface of TiO_2 NPs. At high decomposition temperature, the reaction of CH_2O and NO_2 would provide the main exothermic reaction.

4 Conclusion

Hydrothermal processing was reported to be a beneficial technology that could offer fabrication of highly-crystalline TiO_2 NPs in dispersion. The particle size of the synthesized TiO_2 NPs was found to be ranging from 3.0 to 10.0 nm with an average particle size recorded at 5.0 nm, and the calculated surface area of the prepared TiO_2 NPs was found to be $26.87 \pm 0.36\ m^2/g$. The effective coating of TiO_2 with HMX was conducted via co-precipitation technique. The synthesized TiO_2 NPs demonstrated superior catalytic activity on HMX thermolysis. TiO_2 NPs demonstrated dramatic change in HMX thermal behavior. The endothermic phase change of HMX at 187 °C was decreased by 43.3%. The main outcome of this study is that temperature at maximum heat release rate was decreased by 10 °C with an increase in total heat release rate by 46.7%. At temperature higher than 150 °C, $\dot{\mathbf{O}}\mathbf{H}$ radicals would be evolved from TiO_2 NPs surface. These active radicals will have high ability to abstract hydrogen from HMX structure. TiO_2 NPs catalytic mechanism includes the following: (1) Release of $\dot{\mathbf{O}}\mathbf{H}$ radicals initiating destruction of HMX molecule and (2) Adsorption of released NO_2 to the NPs surface. Therefore, the total heat release would increase significantly. Integration of colloidal TiO_2 NPs into HMX would secure high reactivity.

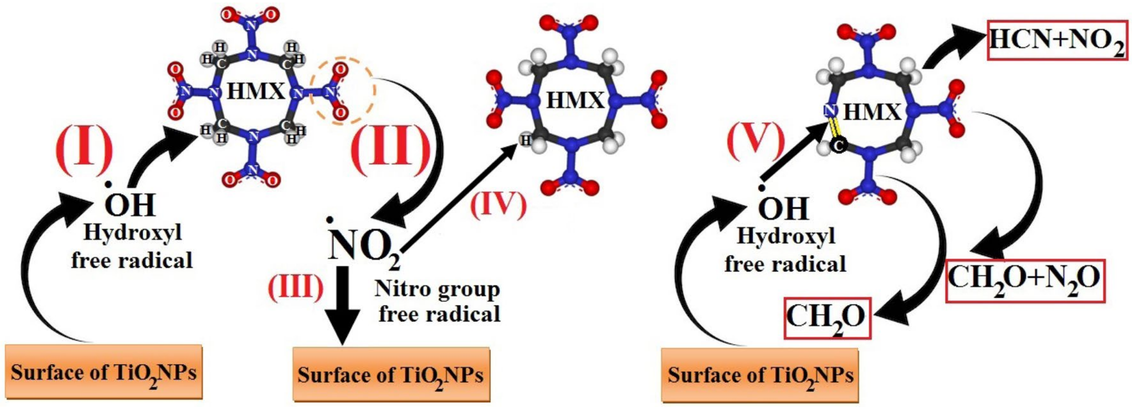

Fig. 11 Catalytic mechanism of TiO_2 NPs on HMX

Funding Not applicable.

Compliance with ethical standards

Conflict of interest The authors declare that they have no conflict of interest.

References

1. M. Meyer, J. Kohler, A. Homburg (eds.), *Explosives*, 6th edn. (Wiley, Weinheim, 2007)
2. F. Monteil-Rivera et al., Dissolution of a new explosive formulation containing TNT and HMX: comparison with octol. J. Hazard. Mater. **174**(1), 281–288 (2010)
3. N. Kubota (ed.), *Propellants and Explosives Thermochemical Aspects of Combustion* (Wiley-VCH, Weinheim, 2002)
4. S. Elbasuney, A. Fahd, H.E. Mostafa, Combustion characteristics of extruded double base propellant based on ammonium perchlorate/aluminum binary mixture. Fuel **208**(Supplement C), 296–304 (2017)
5. S. Elbasuney et al., Chemical stability, thermal behavior, and shelf life assessment of extruded modified double-base propellants. Def. Technol. **14**(1), 70–76 (2018)
6. E.S. Kim, V. Yang, Y.C. Liau, Modeling of HMX/GAP pseudo-propellant combustion. Combust. Flame **131**(3), 227–245 (2002)
7. V.E. Zarko, A.A. Gromov (eds.), *Energetic Nanomaterials Synthesis, Characterization, and Application* (Elsevier, Amsterdam, 2016)
8. Q.-L. Yan et al., Combustion mechanism of double-base propellant containing nitrogen heterocyclic nitroamines (I): the effect of heat and mass transfer to the burning characteristics. Combust. Flame **156**(3), 633–641 (2009)
9. K.V. Meredith, M.L. Gross, M.W. Beckstead, Laser-induced ignition modeling of HMX. Combust. Flame **162**(2), 506–515 (2015)
10. L. Patidar, M. Khichar, S.T. Thynell, Identification of initial decomposition reactions in liquid-phase HMX using quantum mechanics calculations. Combust. Flame **188**, 170–179 (2018)
11. Q.-L. Yan et al., Catalytic effects of nano additives on decomposition and combustion of RDX-, HMX-, and AP-based energetic compositions. Prog. Energy Combust. Sci. **57**, 75–136 (2016)
12. R. Liu, P.W. Chen, Modeling ignition prediction of HMX-based polymer bonded explosives under low velocity impact. Mech. Mater. **124**, 106–117 (2018)
13. A. Singh et al., Thermal decomposition and kinetics of plastic bonded explosives based on mixture of HMX and TATB with polymer matrices. Def. Technol. **13**(1), 22–32 (2017)
14. X.-G. Wu et al., Combustion efficiency and pyrochemical properties of micron-sized metal particles as the components of modified double-base propellant. Acta Astronaut. **68**(7), 1098–1112 (2011)
15. J.J. Xiao et al., Study on structure, sensitivity and mechanical properties of HMX and HMX-based PBXs with molecular dynamics simulation. Comput. Theor. Chem. **999**, 21–27 (2012)
16. A.N. Pivkina et al., Chapter nine—catalysis of HMX decomposition and combustion: defect chemistry approach, in *Energetic Nanomaterials*, ed. by V.E. Zarko, A.A. Gromov (Elsevier, Amsterdam, 2016), pp. 193–230
17. Y. Wang et al., Combustion synthesis of $La_{0.8}Sr_{0.2}MnO_3$ and its effect on HMX thermal decomposition. Chin. J. Chem. Eng. **18**(3), 397–401 (2010)
18. S. Elbasuney, Sustainable steric stabilization of colloidal titania nanoparticles. Appl. Surf. Sci. **409**, 438–447 (2017)
19. M.A. Elsayed, M. Gobara, S. Elbasuney, Instant synthesis of bespoke nanoscopic photocatalysts with enhanced surface area and photocatalytic activity for wastewater treatment. J. Photochem. Photobiol. A **344**, 121–133 (2017)
20. R. Liu et al., Dynamic vacuum stability test method and investigation on vacuum thermal decomposition of HMX and CL-20. Thermochim. Acta **537**, 13–19 (2012)
21. H. Khojasteh et al., Synthesis, characterization and photocatalytic activity of PdO/TiO_2 and Pd/TiO_2 nanocomposites. J. Mater. Sci.: Mater. Electron. **27**(2), 1261–1269 (2016)
22. H. Safajou et al., Enhanced photocatalytic degradation of dyes over graphene/Pd/TiO_2 nanocomposites: TiO_2 nanowires versus TiO_2 nanoparticles. J. Colloid Interface Sci. **498**, 423–432 (2017)
23. A. Abbasi et al., Photo-degradation of methylene blue: photocatalyst and magnetic investigation of Fe_2O_3–TiO_2 nanoparticles and nanocomposites. J. Mater. Sci.: Mater. Electron. **27**(5), 4800–4809 (2016)
24. T. Gholami et al., Photocatalytic degradation of methylene blue on TiO_2@SiO_2 core/shell nanoparticles: synthesis and characterization. J. Mater. Sci.: Mater. Electron. **26**(8), 6170–6177 (2015)
25. H. Safardoust-Hojaghan, M. Salavati-Niasari, Degradation of methylene blue as a pollutant with N-doped graphene quantum dot/titanium dioxide nanocomposite. J. Clean. Prod. **148**, 31–36 (2017)
26. A. Rostami-Vartooni et al., Photocatalytic degradation of azo dyes by titanium dioxide supported silver nanoparticles prepared by a green method using *Carpobrotus acinaciformis* extract. J. Alloys Compd. **689**, 15–20 (2016)
27. M. Sabet, M. Salavati-Niasari, O. Amiri, Using different chemical methods for deposition of CdS on TiO_2 surface and investigation of their influences on the dye-sensitized solar cell performance. Electrochim. Acta **117**, 504–520 (2014)
28. N. Mir, M. Salavati-Niasari, Preparation of TiO_2 nanoparticles by using tripodal tetraamine ligands as complexing agent via two-step sol–gel method and their application in dye-sensitized solar cells. Mater. Res. Bull. **48**(4), 1660–1667 (2013)
29. M. Masjedi et al., Effect of Schiff base ligand on the size and the optical properties of TiO_2 nanoparticles. Superlattices Microstruct. **62**, 30–38 (2013)
30. N. Mir, M. Salavati-Niasari, Effect of tertiary amines on the synthesis and photovoltaic properties of TiO_2 nanoparticles in dye sensitized solar cells. Electrochim. Acta **102**, 274–281 (2013)
31. O. Amiri et al., Stable plasmonic-improved dye sensitized solar cells by silver nanoparticles between titanium dioxide layers. Electrochim. Acta **152**, 101–107 (2015)
32. H. Hou et al., General strategy for fabricating thoroughly mesoporous nanofibers. J. Am. Chem. Soc. **136**(48), 16716–16719 (2014)
33. H. Hou et al., Superior thoroughly mesoporous ternary hybrid photocatalysts of TiO_2/WO_3/gC_3N_4 nanofibers for visible-light-driven hydrogen evolution. J. Mater. Chem. A **4**(17), 6276–6281 (2016)
34. H. Hou et al., Highly efficient photocatalytic hydrogen evolution in ternary hybrid TiO_2/CuO/Cu thoroughly mesoporous nanofibers. ACS Appl. Mater. Interfaces **8**(31), 20128–20137 (2016)
35. H. Hou et al., $BiVO_4$@TiO_2 core–shell hybrid mesoporous nanofibers towards efficient visible-light-driven photocatalytic hydrogen production. J. Mater. Chem. C **7**(26), 7858–7864 (2019)
36. S. Elbasuney, M. Yehia, Ammonium perchlorate encapsulated with TiO_2 nanocomposite for catalyzed combustion reactions. J. Inorg. Organomet. Polym. Mater. **29**(4), 1349–1357 (2019)
37. Z.-X. Wei et al., Combustion synthesis and effect of $LaMnO_3$ and LaOCl powder mixture on HMX thermal decomposition. Thermochim. Acta **499**(1), 111–116 (2010)
38. S. Elbasuney, M. Gobara, M. Yehia, Ferrite nanoparticles: synthesis, characterization, and catalytic activity evaluation for solid rocket propulsion systems. J. Inorg. Organomet. Polym. Mater. **29**(3), 721–729 (2019)

39. R. Dubey et al., Synthesis, characterization and catalytic behavior of Cu nanoparticles on the thermal decomposition of AP, HMX, NTO and composite solid propellants, Part 83. Thermochim. Acta **549**, 102–109 (2012)
40. J. Wei et al., 0D Cu(II) and 1D mixed-valence Cu(I)/Cu(II) coordination compounds based on mixed ligands: syntheses, structures and catalytic thermal decomposition for HMX. Inorg. Chem. Commun. **30**, 13–16 (2013)
41. J.-S. Lee, C.-K. Hsu, C.-L. Chang, A study on the thermal decomposition behaviors of PETN, RDX, HNS and HMX. Thermochim. Acta **392–393**, 173–176 (2002)
42. X. Wang, Y. Li, Selected-control hydrothermal synthesis of α-and β-MnO2 single crystal nanowires. J. Am. Chem. Soc. **124**(12), 2880–2881 (2002)
43. S. Elbasuney, M. Yehia, Thermal decomposition of ammonium perchlorate catalyzed with CuO nanoparticles. Def. Technol. **15**(6), 868–874 (2019)
44. S. Elbasuney, Dispersion characteristics of dry and colloidal nanotitania into epoxy resin. Powder Technol. **268**, 158–164 (2014)
45. S. Elbasuney, Surface engineering of layered double hydroxide (LDH) nanoparticles for polymer flame retardancy. Powder Technol. **277**, 63–73 (2015)
46. S. Elbasuney, Continuous hydrothermal synthesis of AlO(OH) nanorods as a clean flame retardant agent. Particuology **22**, 66–71 (2015)
47. S. Elbasuney, Novel multi-component flame retardant system based on nanoscopic aluminium-trihydroxide (ATH). Powder Technol. **305**, 538–545 (2017)
48. S. Elbasuney, Novel colloidal molybdenum hydrogen bronze (MHB) for instant detection and neutralization of hazardous peroxides. TrAC Trends Anal. Chem. **102**, 272–279 (2018)
49. P. Savage et al., Reactions at supercritical conditions: applications and fundamentals. AIChE J **41**(7), 1723–1778 (1995)
50. K.S. Morley et al., Clean preparation on nanoparticulate metals in porous supports: a supercritical route. J. Chem. Mater. **12**, 1898–1905 (2002)
51. H. Hobbs, Biocatalysis in 'green solvents, in *Chemistry* (University of Nottingham, Notttingham, 2006)
52. S. Elbasuney, Novel colloidal nanothermite particles (MnO_2/Al) for advanced highly energetic systems. J. Inorg. Organomet. Polym. Mater. **28**(5), 1793–1800 (2018)
53. S. Elbasuney et al., Infrared signature of novel super-thermite (Fe_2O_3/Mg) fluorocarbon nanocomposite for effective countermeasures of infrared seekers. J. Inorg. Organomet. Polym. Mater. **28**(5), 1718–1727 (2018)
54. S. Elbasuney et al., Super-thermite (Al/Fe_2O_3) fluorocarbon nanocomposite with stimulated infrared thermal signature via extended primary combustion zones for effective countermeasures of infrared seekers. J. Inorg. Organomet. Polym. Mater. **28**, 2231–2240 (2018)
55. A. Bouvy, A. Opstaele (eds.), *Waterbrone Coating and Additives* (Royal Chemical Society, London, 1995)
56. S. Voyutsky (ed.), *Colloid Chemistry* (Mir Publisher, Moscow, 1978)
57. R.J. Hunter (ed.), *Zeta Potential in Colloid Science* (Academic Press, New York, 1981)
58. S. Elbasuney et al., Stabilized super-thermite colloids: a new generation of advanced highly energetic materials. Appl. Surf. Sci. **419**, 328–336 (2017)
59. J. Lee et al., Titanium dioxide nanoparticles oral exposure to pregnant rats and its distribution. Part. Fibre Toxicol **16**(1), 31 (2019)
60. A.C.S. de la Vega et al., Nanosized titanium dioxide UV filter increases mixture toxicity when combined with parabens. Ecotoxicol. Environ. Saf. **184**, 109565 (2019)
61. L.W. Zhang, N.A. Monteiro-Riviere, Toxicity assessment of six titanium dioxide nanoparticles in human epidermal keratinocytes. Cutan. Ocular Toxicol **38**(1), 66–80 (2019)
62. M. Abd Elkodous et al., Layer-by-layer preparation and characterization of recyclable nanocomposite ($Co_xNi_{1-x}Fe_2O_4$; X = 0.9/SiO_2/TiO_2). J. Mater. Sci.: Mater. Electron. **30**(9), 8312–8328 (2019)
63. Y. Tang et al., Measurement of SnO_2 nanoparticles coating on titanium dioxide nanotube arrays using grazing-incidence X-ray diffraction, in *Characterization of Minerals, Metals, and Materials 2019* (Springer, Berlin, 2019), pp. 703–711
64. H. Fernando et al., Synthesis, characterization and antimicrobial activity of garcinol coated titanium dioxide nanoparticles, in *Proceedings of Annual Scientific Sessions of Faculty of Medical Sciences* (2019)
65. L. Guo et al., In situ generated plasmonic silver nanoparticle-sensitized amorphous titanium dioxide for ultrasensitive photoelectrochemical sensing of formaldehyde. ACS Sens. **4**(10), 2724–2729 (2019)
66. N. El-Shafai et al., Graphene oxide decorated with zinc oxide nanoflower, silver and titanium dioxide nanoparticles: fabrication, characterization, DNA interaction, and antibacterial activity. RSC Adv. **9**(7), 3704–3714 (2019)
67. H. Gao et al., The efficient biogeneration of Ag and NiO nanoparticles from VPLE and a study of the anti-diabetic properties of the extract. RSC Adv. **10**(5), 3005–3012 (2020)
68. M.A. Maksoud et al., Incorporation of Mn^{2+} into cobalt ferrite via sol–gel method: insights on induced changes in the structural, thermal, dielectric, and magnetic properties. J. Sol-Gel. Sci. Technol. **90**(3), 631–642 (2019)
69. A.W. Jatoi, I.S. Kim, Q.-Q. Ni, Cellulose acetate nanofibers embedded with AgNPs anchored TiO_2 nanoparticles for long term excellent antibacterial applications. Carbohydr. Polym. **207**, 640–649 (2019)
70. W.R. Thalgaspitiya et al., A novel, mesoporous molybdenum doped titanium dioxide/reduced graphene oxide composite as a green, highly efficient solid acid catalyst for acetalization. Dalton Trans. **49**, 3786–3795 (2020)
71. A. Nurfadillah, M. Nasir, R.A. Lubis, Synthesis and characterization of sulfonated PVDF TiO_2-natural zeolite nanocomposites membrane, in *Key Engineering Materials* (Trans Tech Publ, 2019)
72. O. Fichera et al., Characterization of water-based paints containing titanium dioxide or carbon black as manufactured nanomaterials before and after atomization. Appl. Nanosci. **9**(4), 515–528 (2019)
73. A.I. El-Batal et al., Nystatin-mediated bismuth oxide nano-drug synthesis using gamma rays for increasing the antimicrobial and antibiofilm activities against some pathogenic bacteria and Candida species. RSC Adv. **10**(16), 9274–9289 (2020)
74. M. Srinivasan et al., Green synthesis and characterization of titanium dioxide nanoparticles (TiO2 NPs) using *Sesbania grandiflora* and evaluation of toxicity in zebrafish embryos. Process Biochem. **80**, 197–202 (2019)
75. H. Pouran et al., Assessment of ATR-FTIR spectroscopy with multivariate analysis to investigate the binding mechanisms of Ag and TiO_2 nanoparticles to Chelex®-100 or Metsorb™ for the DGT technique. Anal. Methods (2020). https://doi.org/10.1039/C9AY02458A
76. T. Munir et al., Impact of silver dopant on structural and optical properties of TiO_2 nanoparticles. DJNB. **14**(2), 279–284 (2019).
77. G.S. El-Sayyad et al., Merits of photocatalytic and antimicrobial applications of gamma-irradiated $Co_xNi_{1-x}Fe_2O_4$/SiO_2/TiO_2; x = 09 nanocomposite for pyridine removal and pathogenic bacteria/fungi disinfection: implication for wastewater treatment. RSC Adv. **10**(9), 5241–5259 (2020)

78. M. Maksoud et al., Controllable synthesis of $Co_{1-x}M_xFe_2O_4$ nanoparticles (M= Zn, Cu, and Mn; x= 0.0 and 0.5) by cost-effective sol-gel approach: analysis of structure, elastic, thermal, and magnetic properties. J. Mater. Sci.: Mater. Electron. (2020). https://doi.org/10.1007/s10854-020-03518-0.pdf
79. M. Arulprakasajothi et al., Heat transfer study of water-based nanofluids containing titanium oxide nanoparticles. Mater. Today: Proc. **2**(4–5), 3648–3655 (2015)
80. H. Lee, S. Jin, S. Yim, Titanium oxide nanoparticle-embedded mesoporous manganese oxide microparticles for supercapacitor electrodes. J. Phys. Chem. Solids **138**, 109264 (2020)
81. W. Sun et al., Synthesis and enhanced electrorheological properties of TS-1/titanium oxide core/shell nanocomposite. Ind. Eng. Chem. Res. **59**(3), 1168–1182 (2020)
82. S. Elbasuney et al., Surface modified colloidal silica nanoparticles: Novel aspect for complete identification of explosive materials. Talanta **211**, 120695 (2020)
83. F.M. Mosallam et al., Biomolecules-mediated synthesis of selenium nanoparticles using Aspergillus oryzae fermented Lupin extract and gamma radiation for hindering the growth of some multidrug-resistant bacteria and pathogenic fungi. Microb Pathog. **122**, 108–116 (2018)
84. M.A. Maksoud et al., Synthesis and characterization of metals-substituted cobalt ferrite [$M_xCo_{(1-x)}Fe_2O_4$;(M= Zn, Cu and Mn; x= 0 and 0.5)] nanoparticles as antimicrobial agents and sensors for Anagrelide determination in biological samples. Mater. Sci. Eng.: C **92**, 644–656 (2018)
85. A. Ashour et al., Antimicrobial activity of metal-substituted cobalt ferrite nanoparticles synthesized by sol–gel technique. Particuology **40**, 141–151 (2018)
86. M. Zhang et al., What occurs in colloidal gas aphron-induced separation of titanium dioxide nanoparticles? Particle fate analysis by tracking technologies. Sci. Total Environ. **716**, 137104 (2020)
87. J.H. Kim et al., Mussel adhesive protein-coated titanium oxide nanoparticles for effective NO removal from versatile substrates. Chem. Eng. J. **378**, 122164 (2019)
88. Q. Wang et al., Superhydrophobic paper fabricated via nanostructured titanium dioxide-functionalized wood cellulose fibers. J. Mater. Sci. **55**(16), 7084–7094 (2020)
89. H. Lee et al., Titanium dioxide modification with cobalt oxide nanoparticles for photocatalysis. J. Ind. Eng. Chem. **32**, 259–263 (2015)
90. J.J.-I. Yoh et al., Test-based thermal explosion model for HMX. Proc. Combust. Inst. **31**(2), 2353–2359 (2007)
91. C.M. Tarver, T.D. Tran, Thermal decomposition models for HMX-based plastic bonded explosives. Combust. Flame **137**(1), 50–62 (2004)